International Journal of Biological Macromolecules 358 (2026) 151719

Contents lists available at ScienceDirect

International Journal of Biological Macromolecules

journal homepage: www.elsevier.com/locate/ijbiomac

Calcium as a molecular switch that regulates Annexin A11 N- and C-terminal domains interaction and its role in ALS

Giulia Di Napoli [a,1], Lorenzo Alfurno [a,1], Alex Fissore [a,1], Eleonora Raccuia [a], Paolo Olivieri [b], Mauro Marengo [a], Simonetta Oliaro-Bosso [a], Fabrizio Dal Piaz [c], Gianluca Catucci [d], Gianfranco Gilardi [d], Adrian Velazquez-Campoy [e,f,g], Filippo Prischi [h], Angela De Simone [a], Francesca Spyrakis [a], Francesco Di Palma [a,i,*], Salvatore Adinolfi [a,**]

[a] Department of Drug Science and Technology, University of Turin, Turin, Italy
[b] Institute of Biochemistry and Biology, Department of Molecular Enzymology, University of Potsdam, D-14476, Potsdam, Germany
[c] Department of Medicine, Surgery and Dentistry, University of Salerno, Baronissi, Italy
[d] Department of Life Sciences and Systems Biology, University of Turin, Turin, Italy
[e] Department of Biochemistry and Molecular and Cellular Biology, School of Sciences, and Institute for Biocomputation and Physics of Complex Systems (BIFI), University of Zaragoza, Zaragoza, Spain
[f] Instituto de Investigación Sanitaria Aragón (IIS Aragón), Zaragoza, Spain
[g] Centro de Investigación Biomédica en Red de Enfermedades Hepáticas y Digestivas (CIBEREHD), Madrid, Spain
[h] Randall Centre for Cell and Molecular Biophysics, King's College London, London, UK
[i] Center for Human Technologies, Istituto Italiano di Tecnologia, Genoa, Italy

ARTICLE INFO

Keywords:
RNA-transport
Annexin A11
Calcium-regulation
Amyotrophic lateral sclerosis

ABSTRACT

Amyotrophic Lateral Sclerosis (ALS) is a fatal neurodegenerative disease marked by progressive motor neuron loss, leading to muscle paralysis and respiratory failure. Genetic mutations, notably in the *ANXA11* gene, have been implicated in both familial and sporadic ALS forms. *ANXA11* functions as a cellular "tether," orchestrating the transport of RNA-protein complexes and lysosomes through its N-terminal (Nt) and C-terminal (Ct) domains, respectively. This study uncovers a novel calcium-dependent regulatory mechanism governing the intramolecular interaction between these domains. Using biochemical, biophysical, and computational approaches, we suggest that in the absence of calcium, *ANXA11* adopts a closed conformation with stable Nt-Ct interactions. Elevated calcium levels induce a conformational shift, disrupting this interaction and exposing binding sites for RNA and membranes. Crucially, we show that the ALS-associated D40G mutation in the Nt domain impairs this calcium-regulated interaction, favoring a persistent open conformation that predisposes to toxic protein aggregation. These findings reveal that calcium acts as a molecular switch modulating *ANXA11* conformation and function, providing new insights into its role in ALS pathogenesis and potential therapeutic targets.

1. Introduction

Amyotrophic Lateral Sclerosis (ALS) is a devastating neurodegenerative disorder characterized by the progressive loss of both upper and lower motor neurons. This degeneration leads to muscle weakness, paralysis, and ultimately, respiratory failure, which is the primary cause of death in affected individuals. Despite extensive research, the precise molecular mechanisms underlying ALS remain incompletely understood, though genetic factors are known to play a significant role (1,2).

In recent years, genetic mutations in different genes have been associated with ALS. Notably, mutations in the ANXA11 gene have emerged as significant contributors to both familial and sporadic forms of the disease.

Recent studies have revealed that ANXA11 serves as a "tether", facilitating transport by connecting motor "vehicles", such as lysosomes,

* Correspondence to: F. Di Palma, Center for Human Technologies, Istituto Italiano di Tecnologia, Genoa, Italy.
** Corresponding author.
E-mail addresses: francesco.dipalma@unito.it (F. Di Palma), salvatore.adinolfi@unito.it (S. Adinolfi).
[1] Indicates first authorship.

https://doi.org/10.1016/j.ijbiomac.2026.151719
Received 23 January 2026; Received in revised form 26 March 2026; Accepted 27 March 2026
Available online 28 March 2026
0141-8130/Crown Copyright © 2026 Published by Elsevier B.V. This is an open access article under the CC BY license (http://creativecommons.org/licenses/by/4.0/).

carrying "hitchhiker" complexes like RNA-protein assemblies (3). Tethers formed by ANXA11 enable the rapid and efficient transfer of materials, including mRNAs, to dendrites or axon terminals (4,5). Specifically, its N-terminal domain (Nt) binds directly to RNA, while the C-terminal domain (Ct) interacts with lysosomes, effectively linking these organelles and cargo together to promote passive intracellular transport vital for neuronal function.

ANXA11 is a 56 kDa widely expressed calcium-dependent phospholipid-binding protein that belongs to the annexin protein superfamily. These proteins are present in every Kingdom, except for Yeast (2). Humans have 12 annexin members: A1-A11 and A13 (2).

Annexins share a highly conserved Ct domain characterized by the presence of four motif repeats, each one able to bind a Ca^{2+} ion. Each annexin motif comprises ~70 amino acids arranged into five α-helices, termed A–E. The loops connecting the AB and DE helical hairpins contain the Ca^{2+} binding site (2,6,7). At variance with the Ct, the annexins Nt has great variability in length and sequence determining the functional specificity of each subfamily (8).

The Annexin A1 (ANXA1) Nt domain has been extensively characterized. It is composed of 40 amino-acids folded in a helix-turn-helix (HtH) able to interact with the C-term domain in the absence of calcium. This latter indeed, when present, induces a conformational change that leads to the release of the Nt domain which becomes available for its functions (9). ANXA11 has, on the other hand, the longest N-terminus of ~200 residues, characterized by a low complexity, due to a sequence enriched in Gly, Tyr, and Pro. Multiple sequence alignment, secondary structure predictions and NMR experiments suggested the presence of a putative helical motif around residues 38 to 59 (10–12), in agreement with a previous investigation of recombinant mouse ANXA11 and human ANXA1. Specifically, in A1, the helix packs against the core domain in the absence of calcium ions, but this interaction is released upon calcium activation, freeing the Nt domain, thus able to promote protein-protein interaction. Interestingly, it was predicted a similar regulation mechanism for the ANXA11 Nt domain (1,11).

Recently, mutations in ANXA11 were identified in patients with familial and sporadic ALS by whole-exome sequencing (1,2). Specifically, mutations in the Nt domain, such as G38R and D40G, have been shown to cause abnormal accumulation of ANXA11-aggregates within motor neurons in postmortem spinal cord tissue (2). These aggregates are indicative of disrupted cellular processes and may contribute to neuronal degeneration.

Despite these findings, the precise pathogenic mechanisms by which ANXA11 mutations contribute to motor neuron degeneration remain unclear. It is hypothesized that impaired tethering of RNA granules and lysosomes—critical for proper mRNA transport and cellular homeostasis—may play a role, potentially leading to neuronal stress and degeneration. Further research is needed to elucidate how these mutations disrupt ANXA11's functions and contribute to ALS pathogenesis.

This study presents, for the first time, a detailed molecular mechanism underlying the interplay between the two ANXA11 domains and how it is regulated by calcium. Additionally, our results reveal that the ALS-associated ANXA11 Nt-D40G (Nt_{D40G}) mutation disrupts inter-domain interactions between the Nt and Ct bypassing calcium regulation, leading to abnormal protein aggregation. These insights enhance our understanding of ALS pathology and could inform the development of therapies aimed at stabilizing ANXA11 interactions, restoring mitigating neurodegeneration.

2. Results

2.1. Structural characterization and calcium ions binding properties of ANXA11 Ct

Before testing ANXA11's Nt and Ct functions, we confirmed their proper folding. Circular dichroism (CD) analysis of the Ct, without the thioredoxin carrier, revealed typical α-helix signals, with minima at 210 and 222 nm (Fig. 1a, black line). K2D2 estimated about 70% α-helix content, aligning with other annexins (13–15). The Nt is mostly disordered with few structured elements (12).

Heating the Ct to 75 °C caused a broad minimum in the CD spectrum, indicating protein aggregation (Fig. 1a, green line). Cooling to 5 °C did not restore the original spectrum (Fig. 1a, dotted line), suggesting irreversible aggregation. Moreover, Differential Scanning Calorimetry (DSC) for the combined protein (Fig. 1b, black line) and thioredoxin alone (Fig. S1) as a control that showed a single peak at 70 °C. The Ct showed two endothermic peaks: peak 1 at 46.5 °C for the Ct and peak 2 at 68.5 °C attributed to Thioredoxin.

2.2. ANXA11 Ct domain binds calcium

To investigate and quantify the Ct ability to bind Ca^{2+}, we performed DSC experiments where the Ct thermal transition was measured in the presence and absence of Ca^{2+} in 10 fold molar excess with respect to ANXA11 Ct. The experiment in presence of Ca^{2+} showed that the melting temperature (Tm) of the Ct domain was slightly elevated (46.97 °C; Fig. 1b, peak 1 red line) compared to the Tm in the absence of calcium (46.53 °C; Fig. 1b, peak 1, black line). To assess calcium binding to the Ct domain, we performed DSC experiments measuring its melting temperature with and without Ca^{2+} (10-fold excess with respect to Ct). Ca^{2+} caused a slight increase in Tm from 46.53 °C to 46.97 °C (Fig. 2b, peak 1, red and black line respectively) and raised enthalpy from 107 to 113 kcal/mol, indicating a Ca^{2+} binding, likely through interactions with outer loops. This effect was specific to Ct, as calcium did not alter Thioredoxin's thermal behavior (Fig. 1b, peak 2, red and black line). To further analyze the calcium binding properties of Ct, we conducted fluorescence experiments with increasing Ca^{2+} (Fig. 1c). The addition of Ca^{2+} induced a quenching up to 25% of the fluorescence intensity at 306 nm supporting that Ca^{2+} directly binds to Ct.

To quantify Ct interaction with Ca^{2+}, we used isothermal titration calorimetry (ITC) that provided accurate measurements of binding affinity, enthalpy, and stoichiometry. The titration with Ca^{2+} revealed biphasic thermograms (Fig. 1d), indicating two distinct binding processes and distinct binding sites. Four binding sites were identified: two high-affinity binding sites with dissociation constant $K_d = 1.8 \pm 0.4$ μM and two moderate-affinity binding sites with $K_d = 38 \pm 8$ μM, as a result of the application of the thermodynamic binding equations shown in the Supplementary Materials (Binding model for calcium binding to annexin A11 and data analysis in ITC). These two groups of calcium-binding sites have different strengths and thermodynamic behaviors. Indeed, all sites bind calcium mainly due to entropy ($-T\Delta S_1 = -8.3$ kcal/mol and $-T\Delta S_2 = -14.9$ kcal/mol) with little or unfavorable contribution from enthalpy ($\Delta H_1 = 0.5$ kcal/mol and $\Delta H_2 = 8.9$ kcal/mol). The discovery of two K_d's for Ca^{2+} binding to Ct suggests that the four sites can be divided into two groups. Although annexins' ability to bind calcium is well known (15), to our knowledge, this study provides the first direct quantification of Ca^{2+} affinity for ANXA11 Ct.

2.3. Nt and Ct domain interaction is calcium dependent

After characterizing the structure and calcium-binding ability of Ct, we wanted to investigate the possible intra-molecular interaction between Nt and Ct of ANXA11. Such intramolecular interactions have been already described for ANXA1 (16,17), but never for ANXA11, which has a longer Nt.

To test this interaction, we used microscale thermophoresis (MST). We labeled ANXA11 Ct with a fluorescent dye and gradually added increasing amounts of the unlabeled Nt (0.75 nM - 25 μM), testing both with and without different Ca^{2+} levels. We observed changes in the fluorescence signal indicating that the Nt and Ct bind with a K_d of about 4.3 ± 2.4 μM in the absence of Ca^{2+} (Fig. 1e, red circles). Upon adding Ca^{2+} at 15- and 30-fold excess with respect to Ct concentration the binding weakened significantly. At 15-fold Ca^{2+} excess, the K_d increased

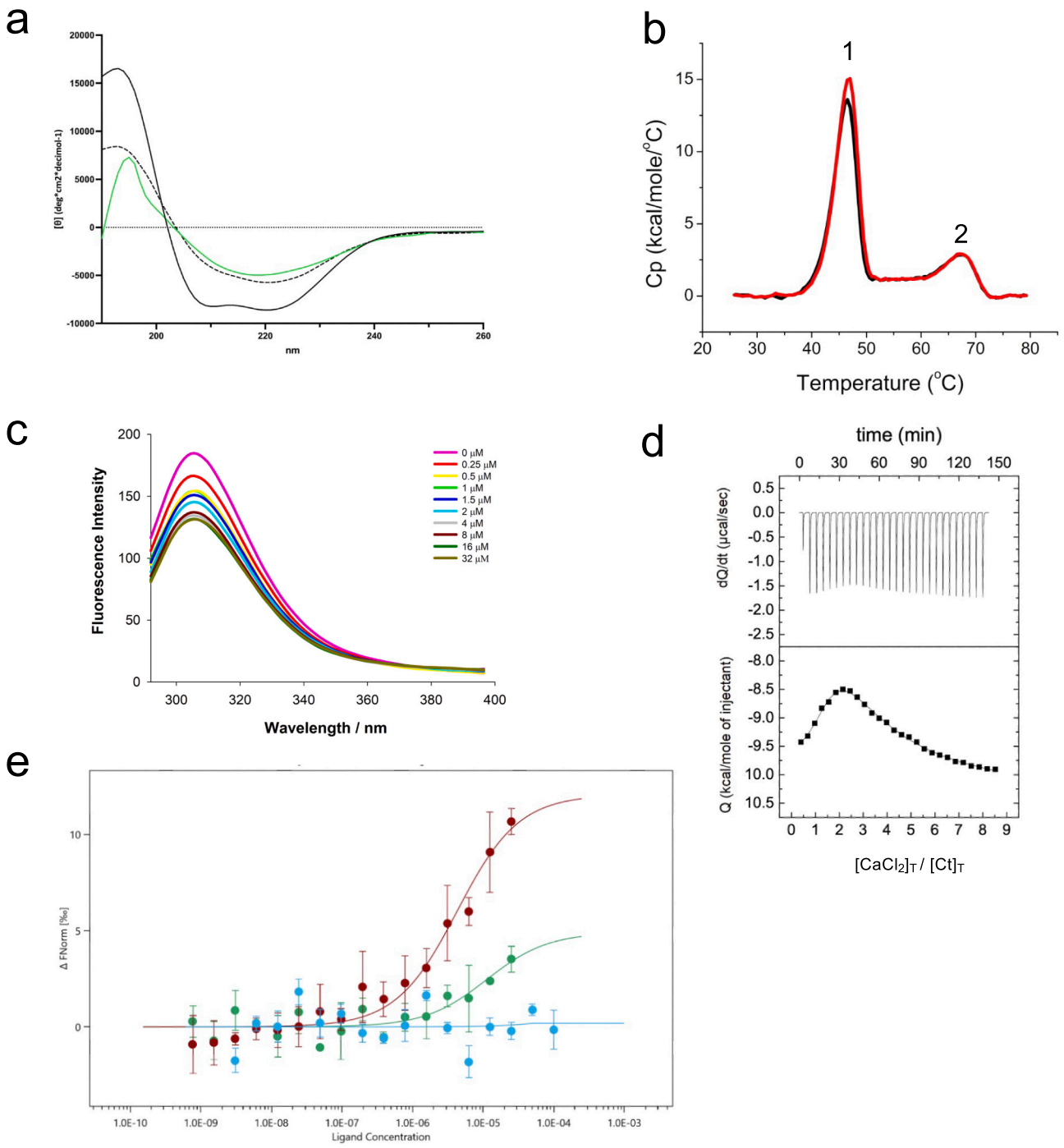

Fig. 1. | **Calcium engagement with ANXA11 Nt and Ct governs its interdomain**. **a**, Far-UV spectra of ANXA11 C-terminal domain: black, 5 °C; green, thermal unfolding at 75 °C; dotted, cooling to 5 °C. **b**, DSC thermogram of C-term in absence (black) and presence (red) of Ca^{2+}; first derivative highlights transition midpoint (T_m = 46.53 °C without Ca^{2+}, 46.97 °C with Ca^{2+}). **c**, Fluorescence spectra of C-term (6 μM) with increasing $CaCl_2$ (0–32 μM, λ_{ex} = 277 nm, 298 K, pH 7.45). **d**, Calorimetric titration of Ca^{2+} (540 μM) binding to ANXA11 C-term (13.5 μM) at 25 °C; top, thermogram; bottom, binding isotherm fitted with the classes of binding sites model. **e**, MST quantification of C—N interaction: normalized fluorescence of labeled proteins titrated with unlabeled N-term at 20 °C; fitting with MO Affinity Analysis v3.0.5.

to around 11.2 ± 4.6 μM, and at 30 times excess, the binding was no longer detectable (Fig. 1e, green and blue circles respectively). These findings indicate that Ca^{2+} disrupts the interaction between the two domains of ANXA11, suggesting that it negatively influences their intramolecular interaction.

To provide a detailed atomistic and dynamic representation of the Nt-Ct interaction, both in the presence and absence of Ca^{2+} ions, we conducted two independent 2.5 μs long molecular dynamics (MD) simulations for the following models: *Nt-Ct-Ca^{2+} (the Ct domain, R191-D505, plus a peculiar helix-turn-helix (HtH) motif of the Nt, I37-G66, plus four bound-Ca^{2+} ions, grey spheres), *Nt-Ct (same model as previous one, without Ca^{2+} ions) and Ct-Ca^{2+} (control model including the Ct domain and the four Ca^{2+} ions).

The root mean square deviation (RMSD) analysis reports on the stability of the Ct (Fig. 2a) and the Nt HtH motif (Fig. 2b) under different conditions. In particular, in the presence of Ca^{2+} ions (Fig. 2a, *Nt-Ct-

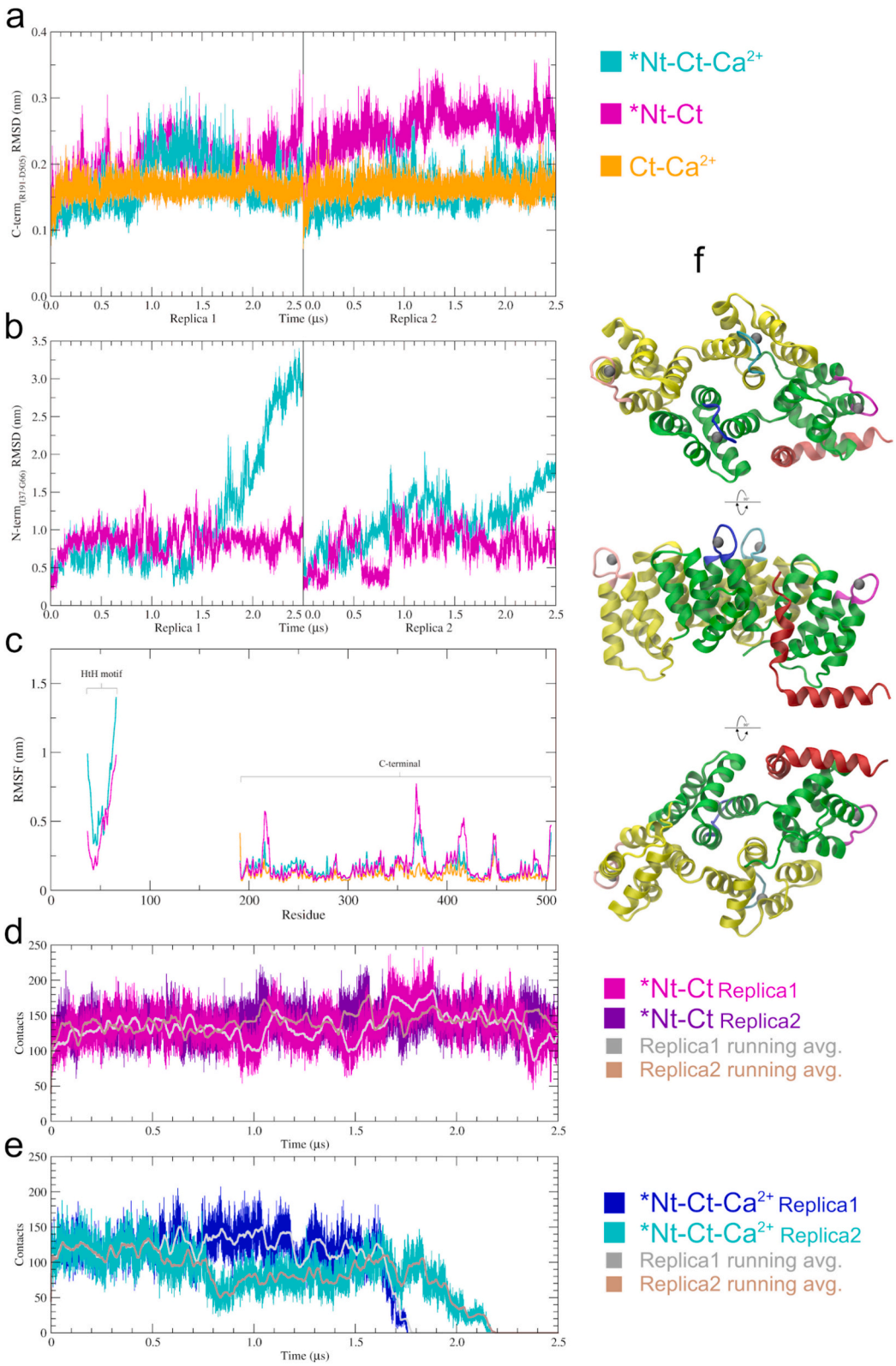

Fig. 2. | **MD analysis of ANXA11 Ct and Nt HtH motif with and without Ca^{2+}.** **a**, RMSD analysis of ANXA11 C-terminal domain for the *Nt-Ct-Ca^{2+} (cyan), the *Nt-Ct (magenta), and the control system, Ct-Ca^{2+} (orange). **b**, RMSD analysis of ANXA11 N-terminal HtH motif when bound to Ct, with and without Ca^{2+} (cyan and magenta, respectively). **c**, RMSF analysis of Nt HtH motif and Ct domain for the three systems: *Nt-Ct-Ca^{2+} (cyan), *Nt-Ct (magenta), and Ct-Ca^{2+} (orange, control); for the last one no HtH is present. **d**, Ct:Nt contact analysis performed for the *Nt-Ct system, in magenta and violet the contact count along Replica1 and 2, respectively, with the related running averages (grey and light-brown). **e**, Ct:Nt contact analysis performed for the *Nt-Ct system *Nt-Ct-Ca^{2+} system, in blue and cyan the contact count along Replica1 and 2, respectively, with the related running averages (grey and brown). **f**, ANXA11 Ct cartoon structure (top, bottom and side views, starting conformation of the *Nt-Ct-Ca^{2+} simulations) in the presence of both the Nt HtH motif and the four Ca^{2+} ions. The repeats forming the Ct domains are coloured green and yellow, the HtH motif in red. The AB loops are highlighted in pink, blue, cyan and magenta. The Ca^{2+} are shown as grey spheres.

Ca^{2+}, cyan curve) the Ct is quite stable in the absence or the presence of the Nt HtH motif (Fig. 2a, Ct-Ca^{2+} and *Nt-Ct-Ca^{2+} systems, cyan and orange curve, respectively). On the contrary, in the *Nt-Ct system (Fig. 2a, magenta line) the RMSD variation reached values above 0.3 nm, highlighting a higher flexibility.

Indeed, in the absence of Ca^{2+} ions, Ct residues in the AB loops (K214-E220, K286-E292, E369-E376, R445-D451 in magenta, blue, pink and cyan respectively in Fig. 2f) fluctuate much more than in the other two systems, as shown by the root mean square fluctuation (RMSF) analysis reported in Fig. 2c. The behavior of the Nt HtH motif is quite peculiar: it remains quite stable in the absence of Ca^{2+} but exhibits huge flexibility in its presence. Indeed, the RMSD of the HtH motif in *Nt-Ct system increases significantly in the second part of the simulations, with respect to that in the *Nt-Ct-Ca^{2+} system (Fig. 2b, magenta and cyan curves, respectively). Accordingly, also the RMSF shows higher values (Fig. 2c). The visual inspection of the MD trajectories show a complete unbinding of the Nt HtH fragment from the Ct, thus suggesting that the presence of Ca^{2+} unfavour Nt-Ct interaction (see Fig. S2a, Videos 1 A/1B). On the contrary, in both replicas of the *Nt-Ct simulations the final structure revealed a bound conformation, with the HtH motif still interacting with the Ct domain (Fig. S2b, Videos 2 A/2B). This is supported by the counting of the Nt-Ct contacts reported in Fig. 2d/e. Indeed, while in the *Nt-Ct system (Fig. 2d), the number of contacts remain stable during the simulation, in the *Nt-Ct-Ca^{2+} system (Fig. 2e) we observe a large reduction of interactions eventually reaching zero when the two domains are completely separate. The control simulations of the Ct-Ca^{2+} confirmed the persisting ions-binding at the AB loop sites (Figs. S3j and S3c).

Our experimental and computational results suggest that ANXA11 exists in two conformations: a compact “close” form where the Nt and Ct interact intramolecularly, and an “open” form where this binding among the two domains is lost, likely allowing for interaction with other molecules. The protein conformations can be further characterized in terms of the molecule radius of gyration (Rg) along the simulations (Fig. S4a); indeed calculating the average Rg of the sampled conformations it is possible to clearly distinguish on a quantitative basis the two states (Fig. S4b). Importantly, this conformational change is Ca^{2+}-dependent and appears to be a key feature of ANXA11's function, facilitating interactions with RNA and lysosomal membranes in the open conformation. This represents the first experimental confirmation of such an intramolecular interaction within the annexin with long Nt.

Based on the results from the MD simulation with the HtH motif, we aimed to verify its binding to the Ct region through a wet-lab approach. We expressed and purified this motif as described in the Materials and Methods. The Ct was labeled with a fluorescent dye and increasing amounts of HtH (from 0.75 nM to 25 μM) were gradually added. We observed changes in the fluorescence signal, indicating that the HtH and Ct interact, with a dissociation constant (Kd) of approximately 5 ± 1 μM in the absence of Ca^{2+} (Fig. S5, green circles). These findings support the evidence from the MD simulations, suggesting that the HtH motif is the main contributor to the interaction between the Ct and Nt regions, as reflected by the similar Kd values measured for the full-length Nt and the HtH motif.

2.4. ANXA11 Nt_{D40G} mutant disrupts the binding with Ct

To understand the role played by ANXA11 in ALS and gather information on the role played by ANXA11 interdomain interaction and within RNA transport, we decided to study the mutation Nt_{D40G} (carrying a single Asp-to-Gly substitution at position 40) identified in ANXA11's Nt domain and found in ALS patients. This mutation is located right at the binding surface between the Nt and Ct domains of ANXA11, allowing us to characterize the binding properties of the Nt p.D40G mutant with the Ct, both with and without Ca^{2+}. These findings are important for understanding how this disease-associated mutation affects ANXA11 physiological function.

We performed MST measurements using 10 nM labeled Ct, titrated with increasing (0.75 nM–25 μM) unlabeled Nt_{D40G}. Fluorescence changes showed little to no binding ($K_d >> 20$ μM, Fig. 3a, green). The wild-type Nt binding curve ($K_d = 4.3 \pm 2.4$ μM) is also shown (Fig. 3a, red) for comparison. To better understand how the Nt_{D40G} mutation within the HtH motif affects the Nt-Ct intradomain interaction, two MD replicas of *Nt_{D40G}-Ct simulations were performed where the Ct did not present the four Ca^{2+} bound. This *Nt_{D40G}-Ct simulation was compared with the *Nt-Ct one carried out previously. This helped us assess the combined impact of the D40G mutation and calcium removal. As expected, RMSD and RMSF analyses of *Nt_{D40G}-Ct showed similar destabilization of the Ct domain's loops observed in the *Nt-Ct, with deviations and fluctuations comparable to previous wild-type simulations without Ca^{2+} (Fig. 3b and 3d vs. Figs. 2a and 2c, magenta curves).

Two new features appeared in the RMSF analysis of the D40G mutant. First, the HtH motif's instability was similar to the *Nt-Ct-Ca^{2+} system (Fig. 3d vs. Fig. 3c, cyan). Second, fluctuations in the first helix (L39-Q48) of the HtH motif were even more pronounced than in other systems (Fig. 3d vs. Fig. 2c, cyan and magenta). Moreover, the residues D249–E257 and Y279 within the Ct showed increased flexibility not observed previously. These Ct residues normally interact with the HtH motif. The acquired flexibility of the mutated HtH, due to the missing Asp at position 40, appears to influence nearby residues on the opposite side of Ct (Fig. 3f structure).

The p.D40G mutation significantly destabilized the HtH-Ct interaction, even without Ca^{2+}, unlike the *Nt-Ct simulations. By the end of *Nt_{D40G}-Ct simulations, contacts dropped to zero (Fig. 3e), and RMSD rose to ~3 nm (Fig. 3c) indicating the complete loss of any intramolecular bond between the two domains; this is also is also reflected in a steep rise in terms of Rg after 1.75 μs, indicating a close-to-open conformational transition (Fig. S4, green panel). Final simulation-sampled conformations (Fig. S3d, Videos 3 A/3B) confirmed the unbinding events. To our knowledge, this is the first experimental and in silico evidence demonstrating a role of this mutation within the ANXA11 function, highlighting that the p.D40G mutant bypasses the essential requirement of Ca^{2+} regulation based on the self-interaction between the Nt and Ct of ANXA11. This loss of regulation leads to the aberrant exposure of the Nt, even when it is not physiologically required, most likely resulting in protein precipitation (18).

3. Discussion

To better understand the role ANXA11 has in ALS and gather molecular evidence regarding the ability of ANXA11 to bind lipid membranes via Ct and RNA via Nt (4), we produced its Nt and Ct domains for individual analysis. These allowed us to investigate the ability of Nt and Ct to interact and how it is regulated by calcium and affected by the Nt_{D40G} mutant, which is linked to ALS.

Structural studies show that Ct is mostly helical, like other annexins, and its stability is increased by the Ca^{2+} binding probably through the interaction with surface loops. While the Ca^{2+}-binding sites in many annexins have been characterized (2,8), direct evidence of Ca^{2+} binding to annexins is scarce (15). We discovered by ITC that Ct has two sets of Ca^{2+}-binding sites with high and moderate affinity, unlike ANXA4, which has uniform calcium binding across its four loops (15).

For the first time in annexins with a long Nt, we examined the role of Ca^{2+} in regulating interactions between the Nt and Ct, providing clear evidence of a direct interaction between these domains that is highly sensitive to Ca^{2+} levels. Specifically, increasing Ca^{2+} concentrations gradually weaken their interaction till the complete dissociation. This indicates that Ca^{2+} functions as a molecular switch: in the absence of Ca^{2+}, the domains interact, thus remaining in a closed conformation; when Ca^{2+} is present, the interaction is disrupted, resulting in an open conformation where both domains are exposed to bind different partners. To confirm this result, it will be necessary to conduct a specific experiment using the full-length ANXA11.

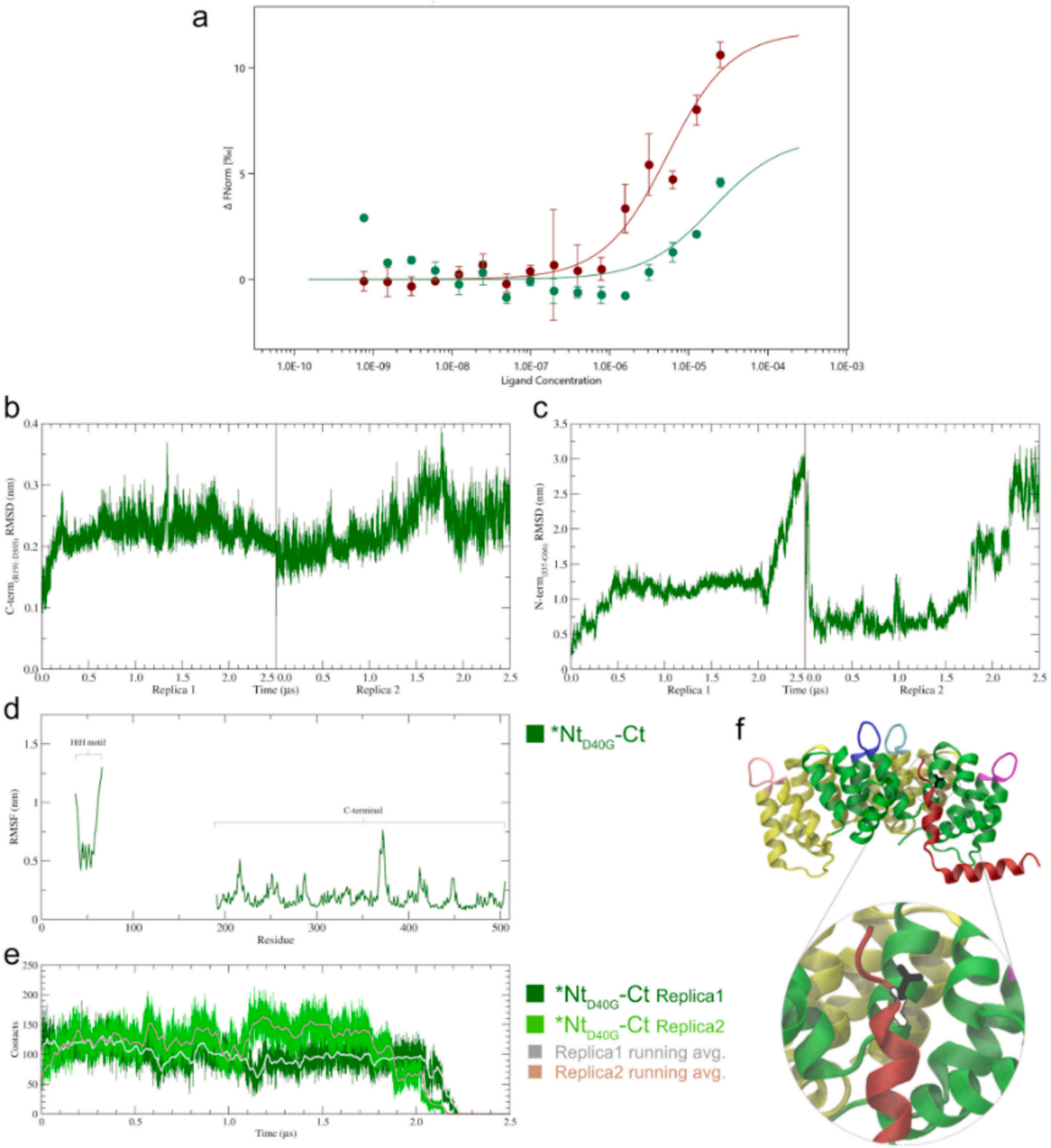

Fig. 3. | **ANXA11 Nt-Ct interaction in the p.D40G mutant and analysis of the related simulations (*Nt$_{D40G}$-Ct). a**, MST quantification of Nt$_{D40G}$-Ct interaction: normalized fluorescence of labeled proteins titrated with unlabeled Nt$_{D40G}$ at 20 °C (green), binding curve of the *wt* Nt shown for comparison (red); fitting with MO Affinity Analysis v3.0.5. **b**, Concerning the *Nt$_{D40G}$-Ct simulations, RMSD analysis of the Ct domain (R191-D505) with respect to the starting structure; the Ct domain sampled distant conformation from the starting one due to the absence of Ca^{2+}, like in *Nt-Ct simulations (Fig. 2a, magenta).**c**, RMSD of the Nt HtH motif (I37-G66) carrying the p.D40G mutation, in the occurrence of an unbinding event in both replicas, HtH motif detaching from the Ct domain, a rapid increase of the deviation is observable. **d**, RMSF analysis of the *Nt$_{D40G}$-Ct simulations: HtH motif and Ct domain are pointed out; even in the absence of Ca^{2+} ions, due to the p.D40G mutation, the fluctuations of the HtH residues are large, in particular the L39-Q48 ones; large fluctuations in the Ct domain can be found at the four AB loop regions, and at residues D249-E257 (D helix) and Y279 that were initially pairing with the HtH. **e**, HtH/Ct contact analysis in the *Nt$_{D40G}$-Ct simulations, in dark- and light-green the contact count along Replica1 and 2, respectively, with the related running averages (grey and light-brown), both sampling the disruption of the interaction between the two domains at ~2.2 μs. **f**, ANXA11 Ct structure (side view, starting conformation of the *Nt$_{D40G}$-Ct simulations) with the interacting HtH (red) carrying the Asp-to-Gly mutation at position 40 (black/white licorice and zoomed in below); such an interaction will be lost during the simulations (Videos 3 A and 3B).

MD simulations confirmed the experimental results adding detailed insights into the Ct:Nt interaction. Without Ca^{2+}, the two domains bind stably. Ca^{2+} in addition to the simulation disrupts the interaction both stabilizing the Ct structure and increasing HtH motif fluctuations. These opposite effects lead to the decoupling of their dynamics leading to their rapid dissociation. This ability to exist in two conformations is crucial for modulating cellular functions, acting as a sensor, and enabling rapid responses to stimuli. Similar mechanisms have been observed in ANXA1, where calcium triggers the release of the short Nt to carry out its specific roles (1). Even if the study of the influence of the disordered portion of the Nt on the HtH:Ct interaction might require further in silico investigation, this is the first documented Ca^{2+} regulatory mechanism for an annexin with a long Nt. It is tempting to suggest it may be a common feature across the annexin family.

Few considerations are needed to discuss the biological relevance of our data. The concentration of free Ca^{2+} within cells varies widely depending on cellular location and conditions (19). Under resting conditions, Ca^{2+} levels typically range from 40 to 100 nM, whereas in the extracellular matrix, they can reach approximately 1–2 mM (20). The Ca^{2+} concentration within intracellular organelles, such as the endoplasmic reticulum (ER), generally ranges between 100 and 500 μM (19).

Considering this information and our calculated dissociation constant (Kd) for the binding between the Ct and Nt domains, we propose a model in which fluctuations in Ca^{2+} levels function as a switch between two functional states of ANXA11. Specifically, during neuronal activation, when Ca^{2+} levels rise, Ca^{2+} binding to the Ct domain would rapidly induce the transition to the "open" conformation. This dynamic process is biologically significant, as ANXA11 must alternate between open and closed conformations. The open state should be stabilized only when binding partners are available, with Ca^{2+} acting as the key regulator orchestrating these conformational shifts.

Discovering the role of Ca^{2+} in the regulation of ANXA11 prompted us to investigate its connection to ALS, with a focus on the Nt_{D40G} mutant, which is associated with toxic protein aggregation, as described in literature (18,21,22). Our data suggest that the loss of Ca^{2+} regulation of the Nt–Ct interaction caused by this mutation may result in a more stable open conformation, in which the Nt residues are more exposed to the solvent. This conformational change could be associated with an increased tendency for protein aggregation (18,22). Although we cannot rule out the possibility that binding partners may also contribute to the tendency to aggregate, the primary effect of the p.D40G mutation in our model appears to be the disruption of the intramolecular interaction between the Ct and Nt domains, independent of the presence of Ca^{2+}. Interactions with other partners are likely to occur only after the Nt and Ct are freed from this intramolecular association. Together, these molecular insights into ANXA11's calcium-dependent conformational regulation and its disruption by ALS-linked mutations provide a mechanistic understanding of how alterations at the protein level may contribute to the pathological protein aggregation and cellular dysfunction observed in ALS.

4. Material and methods

4.1. ANXA11 Nt, Ct and Nt_{D40G} domain production

Variations of previously published purification protocols were used to obtain soluble, highly pure isolated ANXA11 Nt (residues 1–191) domain (12). A modified purification protocol was instead adopted for the Ct (residues 201–505), the Nt_{D40G} mutant (p.D40G mutant, residues 1–191), and the Helix-turn-helix portion (HtH) of the Nt domain (residues 37–70).

The N-terminal (Nt, residues 1–191), C-terminal (Ct, residues 201–505), NtD40G and HtH fragments of ANXA11 were produced as thioredoxin fusion proteins, a strategy employed to enhance protein solubility, using constructs cloned into a pET His6 TEV LIC plasmid. Expression was carried out in *E. coli* BL21 (DE3) cells grown in LB supplemented with 100 μg/mL ampicillin at 37 °C until OD600 reached 0.6, followed by induction with 1 mM IPTG at 20 °C overnight. Cells were lysed in buffer containing 20 mM Tris-HCl pH 7.5, 150 mM NaCl for Ct or 20 mM NaCl for Nt and Nt_{D40G}, 10 mM imidazole, 1 mM DTT, and 1 mM PMSF. Soluble proteins were purified by Ni-NTA chromatography using an elution buffer matching the lysis buffer but containing 300 mM imidazole. For the Ct domain, eluted fractions were collected in tubes supplemented with EDTA to a final concentration of 50 mM. When necessary, the thioredoxin tag was removed by TEV protease digestion overnight at 4 °C during dialysis against SEC buffer (20 mM Tris-HCl pH 7.5, 150 mM NaCl for Ct, and 20 mM NaCl for Nt, HtH and Nt_{D40G}). Proteins were further purified by reverse Ni-NTA chromatography and size-exclusion chromatography on a Sephadex 75 10/300 column. Chromatograms showed a single peak corresponding to the monomeric form of each domain.

4.2. Circular dichroism (CD)

CD spectra were acquired using a Jasco J-815 spectropolarimeter equipped with a Jasco PFD-425S Peltier system. Measurements were performed in a 0.1 mm path length quartz cuvette under a continuous nitrogen 5.5 flow to minimize oxygen interference at wavelengths near 200 nm. Protein samples were prepared at 0.1 mg/mL in 20 mM Hepes buffer, pH 7.5. Spectra were recorded in the 190–260 nm range at a scanning speed of 100 nm/min. Each spectrum represents the average of three consecutive scans. Secondary structure estimation was performed using K2D2 and K2D3 algorithms. Thermal unfolding profiles were recorded by monitoring the CD signal at 222 nm from 5 °C to 75 °C at a heating rate of 1 °C/min. Spectra were collected at 5 °C, 25 °C, 30 °C, 40 °C, 50 °C, 60 °C, and 75 °C.

4.3. Differential scanning calorimetry

The DSC experiments were performed using VP-Capillary DSC, Malvern Instruments Ltd. Worcestershire, UK. The samples were placed in the calorimeter in a 200-μl sample cell against a 200-μl -ml reference cell that was filled with a blank solution consisting of the Ct of protein containing its own buffer. Both tdx-Ct fused protein and thioredoxin were used at 14 μM in all experiments. The cells were equilibrated inside the calorimeter for 10 min at 25 °C before heating up to the final temperature at a given rate. Cycles of cooling and reheating of the samples were performed to obtain the background for buffer subtraction or to test the hypothetical refolding. Replicate runs did not vary more than 0.25 °C. The denaturation temperature T_m and the ΔH were determined by fitting the data with the ORIGIN embedded program suite. To perform the analysis at different scan rates, the cells were pre-equilibrated with at least 10 cycles of buffer in the same setup of the experiment.

4.4. Fluorescence Measurements of the Ct with Ca^{2+}

Fluorescence measurements were performed on a PerkinElmer® LS-55 spectrofluorimeter equipped with a liquid thermostated cell holder set at 25 °C. Excitation was set at 277 nm and emission spectra were recorded from 292 to 400 nm. Protein concentration was 6 μM, scan speed 50 nm/min, with excitation/emission slit widths of 5.0 and 8.0 nm. Protein samples were prepared in 200 μL of buffer (20 mM HEPES, 150 mM NaCl, pH 7.5). Calcium titrations were carried out by successive additions of $CaCl_2$ to reach final concentrations from 0 to 32 μM, without altering protein concentration, and the intrinsic fluorescence of tyrosine residues in the protein structure was used to monitor changes in the microenvironment upon calcium binding (23,24) and each addition, solutions were mixed and spectra acquired. Control experiments were performed by adding equivalent buffer volumes instead of $CaCl_2$.

4.5. Microscale Thermophoresis measurements

The binding affinity between the Ct and Nt domains, as well the interaction with Nt 37–70 (Helix-turn-helix, HtH) and the interaction of the Nt_{D40G} variant with Ct, were investigated by microscale thermophoresis (MST) using a Monolith NT.115 instrument (NanoTemper Technologies, Munich, Germany). Measurements were performed using the Nano Red LED at 100% excitation power and MST power at 40%. Ct was labeled with the Protein Labeling Kit RED-NHS 2nd Generation (MO-L011, NanoTemper Technologies, Munich, Germany), yielding ~7 μM labeled protein with a labeling degree of ~0.6. The Nt-Ct binding was measured using 5 nM labeled Ct and Nt concentrations ranging from 0.75 nM to 25 μM. Nt_{D40G}/Ct and HtH-Ct binding was measured under the same conditions as Ct/Nt. All MST measurements were carried out at 20 °C in 20 mM Tris-HCl and 20 mM NaCl buffer, pH 7.5, with 0.05% Tween-80, and data were analyzed using MO Affinity Analysis software v3.0.5 (NanoTemper Technologies, Munich, Germany).

4.6. Isothermal titration calorimetry measurements

The calorimetric titrations were performed in a VP-ITC microcalorimeter at 25 °C (MicroCal, Malvern-Panalytical, Malvern, UK). A protein solution of 13.5 μM (Ct) in the calorimetric cell was titrated with $CaCl_2$ solutions previously prepared in chemically matched buffer (Tris-HCl 20 mM, NaCl 150 mM, pH 7.5). A $CaCl_2$ solution at a concentration of 540 μM was used as titrant. A series of 4-μL injections were performed with a spacing of 150 s, stirring speed of 500 r.p.m., and reference power of 10 $\mu cal \cdot s^{-1}$. The heat evolved after each ligand injection was obtained from the integral of the calorimetric signal and normalized by the moles of ligand injected. The heat due to the binding reaction was estimated as the difference between the observed heat of reaction and the corresponding heat of dilution by including an adjustable term in the fitting routine accounting for the background injection heat. The experimental data were fitted using a model with two classes of independent binding sites ($n = 2$ per class), reflecting the biphasic nature of the isotherm. The data analysis for ITC was performed with Origin 7.0 (OriginLab).

4.7. Computational model predictions

In the absence of an experimental ANXA11 (UniProt entry P50995) structure, a query on the AlphaFold Protein Structure DB built on AlphaFold 2 (available at https://alphafold.ebi.ac.uk) (25,26) was performed. Then, taking advantage of the recently updated version of the AlphaFold AI model (27) — available as a web server at https://alphafoldserver.com/about — we also predicted ANXA11 structure in the presence of Calcium ions.

By means of the AlphaFold Server different predictions of ANXA11 (from Ile37 to Asp505) were attempted, in the presence of four Ca^{2+} ions and in their absence. Each job (producing five different predicted models) was repeated three times on the platform using a different randomly generated seed, for each chosen molecule combination. This allowed us to make a first comparison between the prediction in the absence of Ca^{2+} ions generated by AlphaFold 2 (obtained from the DB with entry P50995, Fig. S3a), and the predictions by Alphafold 3.

Careful visual investigation of the models was performed to verify the quality of the predictions (e.g. absence of steric clashes, loop conformations, calcium ion coordination). The resulting structures with and without Ca^{2+} ions (Fig. S3b and Scc respectively), represented the best obtained models in terms of predicted template modeling score and interface predicted template modeling score, and led to a different outcome in terms of the occurrence of the quaternary interactions between the Nt and the Ct domain.

In order to shed light on the role of Calcium in ruling the interaction between the Ct domain and the HtH motif of the N-terminal domain), the following models were built and simulated: *Nt-Ct, ANXA11 in the absence of Calcium ions (removing the amino acids from 67 to 190, in order to focus only on the interaction between the HtH motif and the Ct domain); *Nt-Ct-Ca^{2+}, where 4 Calcium ions were added also grafting the so-called AB-loops, coordinating the ions – i.e. Lys214-Asp219 (Ca1, Fig. S2f), Lys286-Asp291 (Ca2, Fig. S2g), Gly368-Asp375 (Ca3, Fig. S2h), Arg445-Lys450 (Ca4, Fig. S2i) – accordingly; Ct-Ca^{2+}, the control model of the Ct domain in the presence of Calcium ions, but in the absence of the Nt HtH motif. Moreover, taking the resulting *Nt-Ct model and removing the side chain of the Asp40, easily replaced by a H atom, the disease-associated p.D40G variant (18) was obtained, thus carrying a glycine in place of an aspartic acid residue at position 40 of the HtH motif in the N-terminal domain, thus named *Nt_{D40G}-Ct.

The choice of including the structured portion only of the Nt domain (i.e. HtH motif) in the models (named as *Nt) actually allowed, in the subsequent MD, to reduce both the noise deriving from a 123 amino acids-long disordered stretch (#67-#190) and the volume of the simulation box, thus the number of solvent molecules. More specifically, their absence, rather than being a limitation, opens up the possibility of directly investigating the effect of the Ca ions on the interplay between the HtH motif and the Ct domain, or better still its regulation in the absence of any other possible minor factor.

4.8. Molecular dynamics simulations

The selected predicted protein models were let explore the conformational space available to them in simulations (via equilibrium MD), with the GROMACS 2024 engine (28); a widespread protocol (29,30) (details in SI) was applied to set up, minimize and equilibrate the systems before the 2.5 μs-long production simulations (2 replicas for each investigated system) using the amber14sb force field (31), the velocity-rescaling thermostat (32) and the stochastic cell rescaling barostat (33).

For the analysis of the trajectories we employed multiple tools: the Gromacs suite (34,35) was used for the RMSD, RMSF, contact analysis and the analysis of the radius of gyration. All the details are provided in SI.

CRediT authorship contribution statement

Giulia Di Napoli: Writing – original draft, Visualization, Methodology, Investigation, Formal analysis, Data curation. **Lorenzo Alfurno:** Writing – original draft, Visualization, Methodology, Investigation, Formal analysis, Data curation. **Alex Fissore:** Visualization, Methodology, Investigation, Formal analysis, Data curation. **Eleonora Raccuia:** Visualization, Resources, Methodology. **Paolo Olivieri:** Investigation, Formal analysis. **Mauro Marengo:** Validation, Data curation. **Simonetta Oliaro-Bosso:** Methodology, Data curation. **Fabrizio Dal Piaz:** Validation. **Gianluca Catucci:** Investigation, Formal analysis, Data curation. **Gianfranco Gilardi:** Validation. **Adrian Velazquez-Campoy:** Formal analysis, Data curation. **Filippo Prischi:** Validation. **Angela De Simone:** Validation, Formal analysis, Data curation. **Francesca Spyrakis:** Validation, Methodology, Funding acquisition, Data curation. **Francesco Di Palma:** Writing – original draft, Validation, Methodology, Formal analysis, Data curation. **Salvatore Adinolfi:** Writing – review & editing, Supervision, Funding acquisition, Conceptualization.

Ethics declaration

Not applicable.

Declaration of competing interest

The authors declare no competing interests.

Acknowledgments

This work was supported, by University of Turin (Ricerca Locale Grants ADIS_RILO_21_01, ADIS_RILO_23_01, ADIS_AUTOF_25_01,

OLIS_RILO_22_02, MARM_RILO_22_05, MARM_RILO_20_04. SPY-F_RILO_24_01, DESA_RILO_24_01.

Research program CN00000013 “National Centre for HPC, Big Data and Quantum Computing”, funded by the Directorial Decree granting funding n1031 of 17.06.2022 using the resources of the PNRR MUR-M4C2-Investment 1, 4-Notice “National Centres” - D.D. n3138 of 16 December 2021.

Computing time was provided by the Data Science and Computation Facility at IIT on the Franklin HPC system under the umbrella of the Framework Agreement of June 26, 2023, between Fondazione Istituto Italiano di Tecnologia and University of Turin.

Appendix A. Supplementary data

Supplementary data to this article can be found online at https://doi.org/10.1016/j.ijbiomac.2026.151719.

Data availability

Data will be made available on request.

References

[1] A. Rosengarth, H. Luecke, A calcium-driven conformational switch of the N-terminal and core domains of annexin A1, J. Mol. Biol. 326 (2003) 1317–1325.
[2] P.D. Smith, S.E. Moss, Structural evolution of the annexin supergene family, Trends Genet. 10 (1994) 241–246.
[3] Y.C. Liao, et al., RNA granules hitchhike on lysosomes for long-distance transport, using annexin A11 as a molecular tether, Cell 179 (2019) 147–164.e20.
[4] J. Salogiannis, S.L. Reck-Peterson, Hitchhiking: A non-canonical mode of microtubule-based transport, Trends Cell Biol. 27 (2017) 141–150.
[5] R. De Pace, S. Ghosh, V.H. Ryan, et al., Messenger RNA transport on lysosomal vesicles maintains axonal mitochondrial homeostasis and prevents axonal degeneration, Nat. Neurosci. 27 (2024) 1087–1102.
[6] S.E. Moss, R.O. Morgan, The annexins, Genome Biol. 5 (2004) 219.
[7] R. Huber, J. Römisch, E.P. Paques, The crystal and molecular structure of human annexin V, an anticoagulant protein that binds to calcium and membranes, EMBO J. 9 (1990) 3867–3874.
[8] V. Gerke, S.E. Moss, Annexins: from structure to function, Physiol. Rev. 82 (2002) 331–371.
[9] V. Gerke, F.N.E. Gavins, M. Geisow, et al., Annexins—a family of proteins with distinctive tastes for cell signaling and membrane dynamics, Nat. Commun. 15 (2024) 1574.
[10] U. Rescher, V. Gerke, Annexins—unique membrane binding proteins with diverse functions, J. Cell Sci. 117 (2004) 2631–2639.
[11] J. Turnay, N. Olmo, M. Gasset, I. Iloro, J.L. Arrondo, M.A. Lizarbe, Calcium-dependent conformational rearrangements and protein stability in chicken annexin A5, Biophys. J. 83 (2002) 2280–2291.
[12] E.F. Dudas, et al., The structural properties of full-length annexin A11, Front. Mol. Biosci. 11 (2024) 1347741.
[13] E. Lecona, et al., Structural and functional characterization of recombinant mouse annexin A11: influence of calcium binding, Biochem. J. 373 (2003) 437–449.
[14] J. Turnay, et al., Structure–function relationship in annexin A13, the founder member of the vertebrate family of annexins, Biochem. J. 389 (2005) 899–911.
[15] S. Di Micco, et al., Computational, crystallographic, and biophysical characterizations provide insights into calcium and phosphate binding by human annexin A4, Int. J. Biol. Macromol. 308 (2025) 142600.
[16] A. Rosengarth, V. Gerke, H. Luecke, X-ray structure of full-length annexin 1 and implications for membrane aggregation, J. Mol. Biol. 306 (2001) 489–498.
[17] A. Rosengarth, H. Luecke, Annexin A1 crystal structure: Interaction of annexins with membranes, in: J. Bandorowicz-Pikula (Ed.), Annexins: Biological Importance and Annexin-Related Pathologies, Springer Science & Business Media, 2003, pp. 114–126.
[18] B.N. Smith, S.D. Topp, et al., Mutations in the vesicular trafficking protein annexin A11 are associated with amyotrophic lateral sclerosis, Sci. Transl. Med. 9 (2017) eaad9157.
[19] R. Bagur, G. Hajnóczky, Intracellular Ca^{2+} sensing: its role in calcium homeostasis and signaling, Mol. Cell 66 (2017) 780–788.
[20] R.D. Burgoyne, Neuronal calcium sensor proteins: generating diversity in neuronal Ca^{2+} signalling, Nat. Rev. Neurosci. 8 (2007) 182–193.
[21] P.A.G. Lillebøstad, et al., Structure of the ALS mutation target annexin A11 reveals a stabilising N-terminal segment, Biomolecules 10 (2020) 660.
[22] M. Nahm, et al., ANXA11 mutations in ALS cause dysregulation of calcium homeostasis and stress granule dynamics, Sci. Transl. Med. 12 (2020) eaax3993.
[23] N.G. Zhdanova, E.G. Maksimov, A.M. Arutyunyan, V.V. Fadeev, E.A. Shirshin, Tyrosine fluorescence probing of conformational changes in tryptophan-lacking domain of albumins, Spectrochim. Acta A Mol. Biomol. Spectrosc. 174 (2017) 223–229.
[24] A. Sillen, et al., Mechanism of fluorescence and conformational changes of the sarcoplasmic calcium-binding protein of the sand worm Nereis diversicolor upon Ca^{2+} or Mg^{2+} binding, Biophys. J. 85 (2003) 1882–1893.
[25] J. Jumper, et al., Highly accurate protein structure prediction with AlphaFold, Nature 596 (2021) 583–589.
[26] K. Tunyasuvunakool, et al., Highly accurate protein structure prediction for the human proteome, Nature 596 (2021) 590–596.
[27] J. Abramson, J. Adler, J. Dunger, et al., Accurate structure prediction of biomolecular interactions with AlphaFold 3, Nature 630 (2024) 493–500.
[28] S. Páll, M.J. Abraham, C. Kutzner, B. Hess, E. Lindahl, Tackling exascale software challenges in molecular dynamics simulations with GROMACS, in: S. Markidis, E. Laure (Eds.), Solving Software Challenges for Exascale, Lecture Notes in Computer Science, vol. 8759, Springer, Cham, 2015, pp. 3–27.
[29] S. Majumdar, F. Di Palma, F. Spyrakis, S. Decherchi, A. Cavalli, Molecular dynamics and machine learning give insights on the flexibility–activity relationships in tyrosine kinome, J. Chem. Inf. Model. 63 (2023) 4814–4826.
[30] N. Scarano, et al., New insights into the LANCL2-ABA binding mode towards the evaluation of new LANCL agonists, Pharmaceutics 15 (2023) 2754.
[31] J.A. Maier, C. Martinez, K. Kasavajhala, L. Wickstrom, K.E. Hauser, C. Simmerling, ff14SB: improving the accuracy of protein side chain and backbone parameters from ff99SB, J. Chem. Theory Comput. 11 (2015) 3696–3713.
[32] H.J.C. Berendsen, J.R. Grigera, T.P. Straatsma, The missing term in effective pair potentials, J. Phys. Chem. 91 (1987) 6269–6271.
[33] G. Bussi, D. Donadio, M. Parrinello, Canonical sampling through velocity rescaling, J. Chem. Phys. 126 (2007) 014101.
[34] M. Bernetti, G. Bussi, Pressure control using stochastic cell rescaling, J. Chem. Phys. 153 (2020) 114107.
[35] M.J. Abraham, et al., GROMACS: high performance molecular simulations through multi-level parallelism from laptops to supercomputers, SoftwareX 1–2 (2015) 19–25.